EUROPEAN ORGANIZATION FOR NUCLEAR RESEARCH (CERN)

CERN-EP-2022-245
2023/02/03

CMS-TOP-20-008

Measurement of the top quark mass using a profile likelihood approach with the lepton+jets final states in proton-proton collisions at $\sqrt{s} = 13\,\text{TeV}$

The CMS Collaboration

Abstract

The mass of the top quark is measured in $36.3\,\text{fb}^{-1}$ of LHC proton-proton collision data collected with the CMS detector at $\sqrt{s} = 13\,\text{TeV}$. The measurement uses a sample of top quark pair candidate events containing one isolated electron or muon and at least four jets in the final state. For each event, the mass is reconstructed from a kinematic fit of the decay products to a top quark pair hypothesis. A profile likelihood method is applied using up to five observables to extract the top quark mass. The top quark mass is measured to be $171.77 \pm 0.37\,\text{GeV}$. This approach significantly improves the precision over previous measurements.

Submitted to the European Physical Journal C

1 Introduction

The top quark [1, 2] is the most massive fundamental particle and its mass, m_t, is an important free parameter of the standard model (SM) of particle physics. Because of its large Yukawa coupling, the top quark dominates the higher-order corrections to the Higgs boson mass and a precise determination of m_t sets strong constraints on the stability of the electroweak vacuum [3, 4]. In addition, precise measurements of m_t can be used to test the internal consistency of the SM [5–7].

At the CERN LHC, top quarks are produced predominantly in quark-antiquark pairs ($t\bar{t}$) which decay almost exclusively into a bottom (b) quark and a W boson. Each $t\bar{t}$ event can be classified by the subsequent decay of the W bosons. For this paper, the lepton+jets channel is analyzed, where one W boson decays hadronically, and the other leptonically. Hence, the minimal final state consists of a muon or electron, at least four jets, and one undetected neutrino. This includes events where a muon or electron from a tau lepton decay passes the selection criteria.

The mass of the top quark has been measured with increasing precision using the reconstructed invariant mass of different combinations of its decay products [8]. The measurements by the Tevatron collaborations led to a combined value of $m_t = 174.30 \pm 0.65\,\text{GeV}$ [9], while the ATLAS and CMS Collaborations measured $m_t = 172.69 \pm 0.48\,\text{GeV}$ [10] and $m_t = 172.44 \pm 0.48\,\text{GeV}$ [11], respectively, from the combination of their most precise results at $\sqrt{s} = 7$ and 8 TeV (Run 1). The LHC measurements achieved a relative precision on m_t of 0.28%. These analyses extract m_t by comparing data directly to Monte Carlo simulations for different values of m_t. An overview of the discussion of this mass definition and its relationship to a theoretically well-defined parameter is presented in Ref. [12].

In the lepton+jets channel, m_t was measured by the CMS Collaboration with proton-proton (pp) collision data at $\sqrt{s} = 13\,\text{TeV}$. The result of $m_t = 172.25 \pm 0.63\,\text{GeV}$ [13] was extracted using the ideogram method [14, 15], which had previously been employed in Run 1 [11]. In contrast to the Run 1 analysis, in the analysis of $\sqrt{s} = 13\,\text{TeV}$ data, the renormalization and factorization scales in the matrix-element (ME) calculation and the scales in the initial- and final-state parton showers (PS) were varied separately, in order to evaluate the corresponding systematic uncertainties. In addition, the impacts of extended models of color reconnection (CR) were evaluated. These models were not available for the Run 1 measurements and their inclusion resulted in an increase in the systematic uncertainty [13].

In this paper, we use a new mass extraction method on the same data, corresponding to $36.3\,\text{fb}^{-1}$, that were used in Ref. [13]. In addition to developments in the mass extraction technique, the reconstruction and calibration of the analyzed data have been improved, and updated simulations are used. For example, the underlying event tune CP5 [16] and the jet flavor tagger DEEPJET [17] were not available in the former analysis on the data. The new analysis employs a kinematic fit of the decay products to a $t\bar{t}$ hypothesis. For each event, the best matching assignment of the jets to the decay products is used. A profile likelihood fit is performed using up to five different observables, which are used to constrain the main sources of systematic uncertainty. The model for the likelihood incorporates the effects of variations of these sources, represented by nuisance parameters based on simulation, as well as the finite size of the simulated samples. This reduces the influence of systematic uncertainties in the measurement. Tabulated results are provided in the HEPData record for this analysis [18].

2 The CMS detector and event reconstruction

The central feature of the CMS apparatus is a superconducting solenoid of 6 m internal diameter, which provides a magnetic field of 3.8 T. Within the solenoid volume are a silicon pixel and strip tracker, a lead tungstate crystal electromagnetic calorimeter (ECAL), and a brass and scintillator hadron calorimeter (HCAL), each composed of a barrel and two endcap sections. Forward calorimeters extend the pseudorapidity (η) coverage provided by the barrel and endcap detectors. Muons are measured in gas-ionization detectors embedded in the steel flux-return yoke outside the solenoid. A more detailed description of the CMS detector, together with a definition of the coordinate system used and the relevant kinematic variables, can be found in Ref. [19].

The primary vertex is taken to be the vertex corresponding to the hardest scattering in the event, evaluated using tracking information alone, as described in Section 9.4.1 of Ref. [20]. The particle-flow (PF) algorithm [21] aims to reconstruct and identify each individual particle in an event, with an optimized combination of information from the various elements of the CMS detector. The energy of photons is obtained from the ECAL measurement. The energy of electrons is determined from a combination of the electron momentum at the primary interaction vertex as determined by the tracker, the energy of the corresponding ECAL cluster, and the energy sum of all bremsstrahlung photons spatially compatible with originating from the electron track. The energy of muons is obtained from the curvature of the corresponding track. The energy of charged hadrons is determined from a combination of their momentum measured in the tracker and the matching ECAL and HCAL energy deposits, corrected for the response function of the calorimeters to hadronic showers. Finally, the energy of neutral hadrons is obtained from the corresponding corrected ECAL and HCAL energy deposits.

Jets are clustered from PF candidates using the anti-k_{T} algorithm with a distance parameter of 0.4 [22, 23]. The jet momentum is determined as the vectorial sum of all particle momenta in the jet, and is found from simulation to be, on average, within 5 to 10% of the true momentum over the whole transverse momentum (p_{T}) spectrum and detector acceptance. Additional pp interactions within the same or nearby bunch crossings (pileup) can contribute additional tracks and calorimetric energy depositions, increasing the apparent jet momentum. To mitigate this effect, tracks identified as originating from pileup vertices are discarded and an offset correction is applied to correct for remaining contributions. Jet energy corrections are derived from simulation studies so that the average measured energy of jets becomes identical to that of particle level jets. In situ measurements of the momentum balance in dijet, photon+jet, Z+jet, and multijet events are used to determine any residual differences between the jet energy scale in data and in simulation, and appropriate corrections are made [24]. Additional selection criteria are applied to each jet to remove jets potentially dominated by instrumental effects or reconstruction failures. The jet energy resolution amounts typically to 15–20% at 30 GeV, 10% at 100 GeV, and 5% at 1 TeV [24]. Jets originating from b quarks are identified using the DEEPJET algorithm [17, 25, 26]. This has an efficiency of approximately 78%, at a misidentification probability for light-quark and gluon jets of 1% [17, 26].

The missing transverse momentum vector, $\vec{p}_{\mathrm{T}}^{\,\mathrm{miss}}$, is computed as the negative vector sum of the transverse momenta of all the PF candidates in an event, and its magnitude is denoted as $p_{\mathrm{T}}^{\mathrm{miss}}$ [27]. The $\vec{p}_{\mathrm{T}}^{\,\mathrm{miss}}$ is modified to account for corrections to the energy scale of the reconstructed jets in the event.

The momentum resolution for electrons with $p_{\mathrm{T}} \approx 45\,\mathrm{GeV}$ from $\mathrm{Z} \to \mathrm{ee}$ decays ranges from 1.6 to 5.0%. It is generally better in the barrel region than in the endcaps, and also depends on the bremsstrahlung energy emitted by the electron as it traverses the material in front of the

ECAL [28, 29].

Muons are measured in the pseudorapidity range $|\eta| < 2.4$, with detection planes made using three technologies: drift tubes, cathode strip chambers, and resistive plate chambers. Matching muons to tracks measured in the silicon tracker results in a relative transverse momentum resolution, for muons with p_T up to 100 GeV, of 1% in the barrel and 3% in the endcaps. The p_T resolution in the barrel is better than 7% for muons with p_T up to 1 TeV [30].

3 Data samples and event selection

The analyzed data sample has been collected with the CMS detector in 2016 at a center-of-mass energy $\sqrt{s} = 13$ TeV. It corresponds to an integrated luminosity of 36.3 fb^{-1} [31]. Events are required to pass a single-electron trigger with a p_T threshold for isolated electrons of 27 GeV or a single-muon trigger with a minimum threshold on the p_T of an isolated muon of 24 GeV [32].

Simulated $\mathrm{t\bar{t}}$ signal events are generated with the POWHEG v2 ME generator [33–35], PYTHIA8.219 PS [36], and use the CP5 underlying event tune [16] with top quark mass values, m_t^{gen}, of 169.5, 172.5, and 175.5 GeV. To model parton distribution functions (PDFs), the NNPDF3.1 next-to-next-to-leading order (NNLO) set [37, 38] is used with the strong coupling constant set to $\alpha_S = 0.118$. The various background samples are simulated with the same ME generators and matching techniques [39–43] as in Ref. [13]. The background processes are W/Z+jets, single-top, diboson, and events composed uniquely of jets produced through the strong interaction, referred to as quantum chromodynamics (QCD) multijet events. The PS simulation and hadronization is performed with PYTHIA8, using the CUETP8M1 tune [44].

All of the simulated samples are processed through a full simulation of the CMS detector based on GEANT4 [45] and are normalized to their predicted cross section described in Refs. [46–49]. The effects of pileup are included in the simulation and the events are weighted to match their distribution observed in the data. The jet energy response and resolution in simulated events are corrected to match the data [24]. In addition, the b-jet identification (b tagging) efficiency and misidentification rate [25], and the lepton trigger and reconstruction efficiencies are corrected in simulation [28, 30].

Events are selected with exactly one isolated electron (muon) with $p_T > 29$ (26) GeV and $|\eta| < 2.4$ that is separated from PF jet candidates with $\Delta R = \sqrt{(\Delta\eta)^2 + (\Delta\phi)^2} > 0.3$ (0.4), where $\Delta\eta$ and $\Delta\phi$ are the differences in pseudorapidity and azimuth (in radians) between the jet and lepton candidate. The four leading jet candidates in each event are required to have $p_T > 30$ GeV and $|\eta| < 2.4$. Only these four jets are used in further reconstruction. Exactly two b-tagged jets are required among the four selected jets, yielding 287 842 (451 618) candidate events in the electron+jets (muon+jets) decay channel.

To check the compatibility of an event with the $\mathrm{t\bar{t}}$ hypothesis, and to improve the resolution of the reconstructed quantities, a kinematic fit [50] is performed. For each event, the inputs to the algorithm are the four-momenta of the lepton and of the four leading jets, $\vec{p}_T^{\,miss}$, and the resolutions of these variables. The fit constrains these quantities to the hypothesis that two heavy particles of equal mass are produced, each one decaying to a b quark and a W boson, with the invariant mass of the latter constrained to 80.4 GeV. The kinematic fit then minimizes $\chi^2 \equiv (\mathbf{x} - \mathbf{x}^m)^T G (\mathbf{x} - \mathbf{x}^m)$ where $\mathbf{x}^m$ and $\mathbf{x}$ are the vectors of the measured and fitted momenta, respectively, and G is the inverse covariance matrix, which is constructed from the uncertainties in the measured momenta. The two b-tagged jets are candidates for the b quarks in the $\mathrm{t\bar{t}}$ hypothesis, while the two jets that are not b tagged serve as candidates for the

light quarks from the hadronically decaying W boson. This leads to two possible parton-jet assignments with two solutions for the longitudinal component of the neutrino momentum and four different permutations per event. For simulated $\mathrm{t\bar{t}}$ events, the parton-jet assignments can be classified as correct permutations, wrong permutations, and unmatched permutations, where, in the latter case, at least one quark from the $\mathrm{t\bar{t}}$ decay is not unambiguously matched within a distance of $\Delta R < 0.4$ to any of the four selected jets.

The goodness-of-fit probability, $P_{\mathrm{gof}} = \exp(-\chi^2/2)$, is used to determine the most likely parton-jet assignment. For each event, the observables from the permutation with the highest P_{gof} value are the input to the m_{t} measurement. In addition, the events are categorized as either $P_{\mathrm{gof}} < 0.2$ or $P_{\mathrm{gof}} > 0.2$, matching the value chosen in Ref. [13]. Requiring $P_{\mathrm{gof}} > 0.2$ yields 87 265 (140 362) $\mathrm{t\bar{t}}$ candidate events in the electron+jets (muon+jets) decay channel and has a predicted signal fraction of 95%. This selection improves the fraction of correctly reconstructed events from 20 to 47%. Figure 1 shows the distribution of the invariant mass of the hadronically decaying top quark candidate before ($m_{\mathrm{t}}^{\mathrm{reco}}$) and after ($m_{\mathrm{t}}^{\mathrm{fit}}$) the $P_{\mathrm{gof}} > 0.2$ selection and the kinematic fit. A large part of the depicted uncertainties on the expected event yields are correlated. Hence, the overall normalization of the simulation agrees within the uncertainties, although the simulation predicts 10% more events in all distributions. For the final measurement, the simulation is normalized to the number of events observed in data.

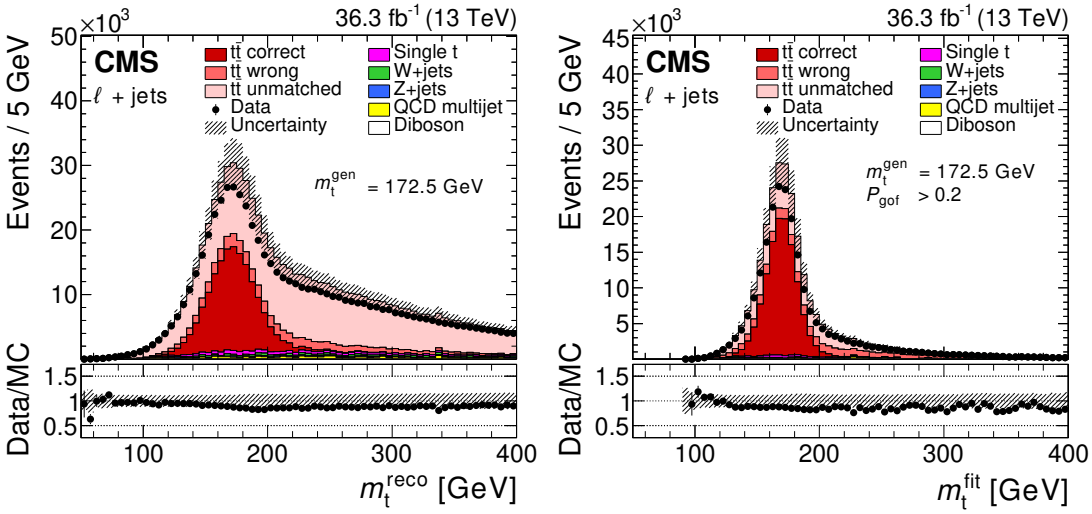

Figure 1: The top quark mass distribution before (left) and after (right) the $P_{\mathrm{gof}} > 0.2$ selection and the kinematic fit. For the simulated $\mathrm{t\bar{t}}$ events, the jet-parton assignments are classified as correct, wrong, and unmatched permutations, as described in the text. The uncertainty bands contain statistical uncertainties in the simulation, normalization uncertainties due to luminosity and cross section, jet energy correction uncertainties, and all uncertainties that are evaluated from event-based weights. A large part of the depicted uncertainties on the expected event yields are correlated. The lower panels show the ratio of data to the prediction. A value of $m_{\mathrm{t}}^{\mathrm{gen}} = 172.5\,\mathrm{GeV}$ is used in the simulation.

4 Observables and systematic uncertainties

For events with $P_{\mathrm{gof}} > 0.2$, the mass of the top quark candidates from the kinematic fit, $m_{\mathrm{t}}^{\mathrm{fit}}$, shows a very strong dependence on m_{t} and is the main observable in this analysis. For events with $P_{\mathrm{gof}} < 0.2$, the invariant mass of the lepton and the b-tagged jet assigned to the semileptonically decaying top quark, $m_{\ell\mathrm{b}}^{\mathrm{reco}}$, is shown in Fig. 2 (right). For most $\mathrm{t\bar{t}}$ events, a low P_{gof}

value is caused by assigning a wrong jet to the W boson candidate, while the two b-tagged jets are the correct candidates for the b quarks. Hence, $m_{\ell b}^{\text{reco}}$ preserves a good m_t dependence and adds additional sensitivity to the measurement. While a similar observable has routinely been used in m_t measurements in the dilepton channel [51, 52], this is the first application of this observable in the lepton+jets channel.

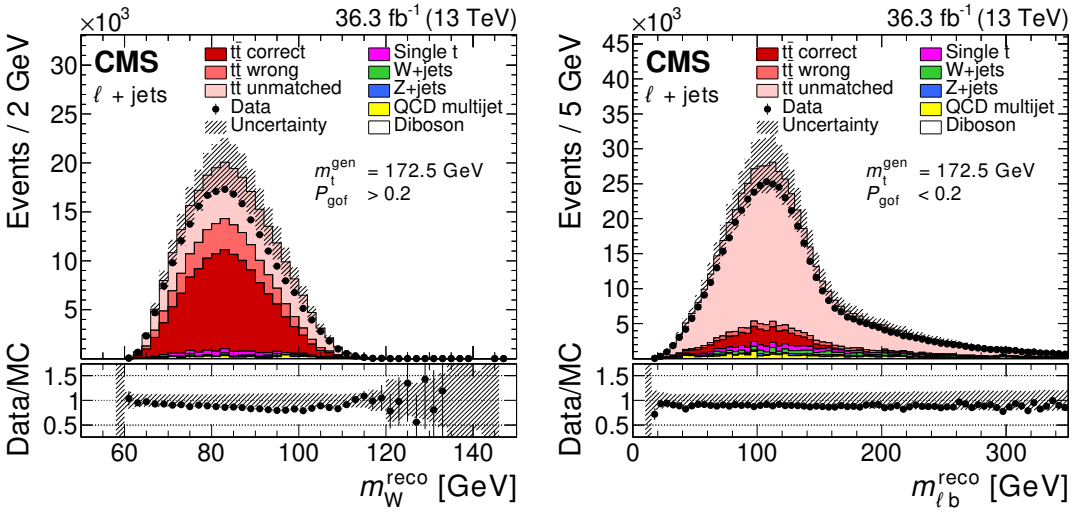

Figure 2: The distributions of the reconstructed W boson mass for the $P_{\text{gof}} > 0.2$ category (left) and of the invariant mass of the lepton and the jet assigned to the semileptonic decaying top quark for the $P_{\text{gof}} < 0.2$ category (right). The uncertainty bands contain statistical uncertainties in the simulation, normalization uncertainties due to luminosity and cross section, jet energy correction uncertainties, and all uncertainties that are evaluated from event-based weights. A large part of the depicted uncertainties on the expected event yields are correlated. The lower panels show the ratio of data to the prediction. A value of $m_t^{\text{gen}} = 172.5\,\text{GeV}$ is used in the simulation.

Additional observables are used in parallel for the mass extraction to constrain systematic uncertainties. In previous analyses by the CMS Collaboration in the lepton+jets channel [11, 13], the invariant mass of the two untagged jets before the kinematic fit, m_W^{reco}, has been used together with m_t^{fit}, mainly to reduce the uncertainty in the jet energy scale and the jet modeling. Its distribution is shown in Fig. 2 (left). As m_W^{reco} is only sensitive to the energy scale and modeling of light flavor jets, two additional observables are employed to improve sensitivity to the scale and modeling of jets originating from b quarks. These are the ratio $m_{\ell b}^{\text{reco}}/m_t^{\text{fit}}$, and the ratio of the scalar sum of the transverse momenta of the two b-tagged jets (b1, b2), and the two non-b-tagged jets (q1, q2), $R_{bq}^{\text{reco}} = (p_T^{b1} + p_T^{b2})/(p_T^{q1} + p_T^{q2})$. Their distributions are shown in Fig. 3. While m_t^{fit} and m_W^{reco} have been used by the CMS Collaboration in previous analyses in the lepton+jets channel, $m_{\ell b}^{\text{reco}}$, $m_{\ell b}^{\text{reco}}/m_t^{\text{fit}}$, and R_{bq}^{reco} are new additions. However, R_{bq}^{reco} has been used in the lepton+jets channel by the ATLAS Collaboration [10, 53].

The distributions of the five observables are affected by uncertainties in the modeling and the reconstruction of the simulated events. These sources of systematic uncertainties are identical to those in the previous measurements [13, 54]. They are summarized in the categories listed below.

- *Method calibration:* In the previous measurements [13, 54], the limited size of the simulated samples for different values of m_t^{gen} lead to an uncertainty in the calibration

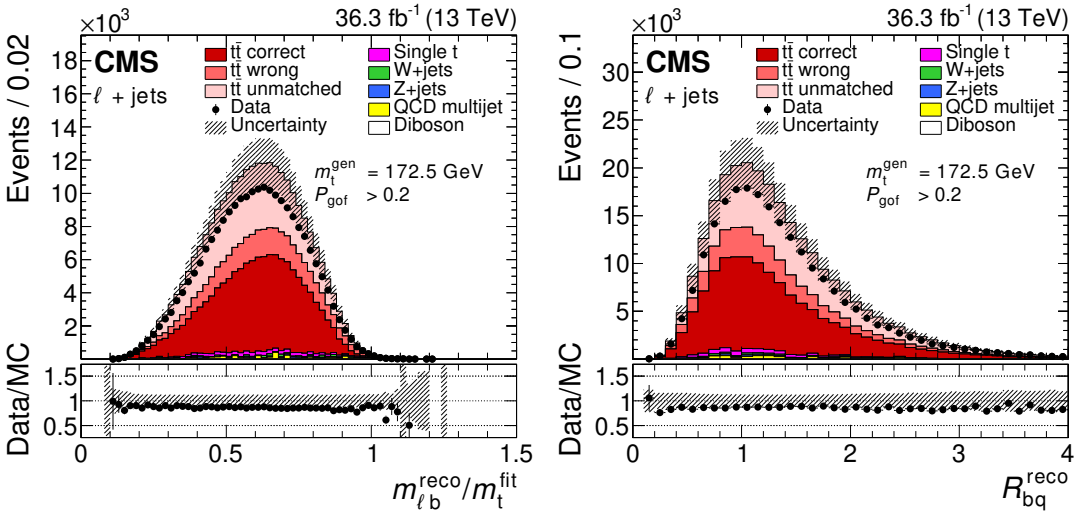

Figure 3: The distributions of $m_{\ell b}^{\text{reco}}/m_{t}^{\text{fit}}$ (left) and of R_{bq}^{reco} (right), both for the $P_{\text{gof}} > 0.2$ category. The uncertainty bands contain statistical uncertainties in the simulation, normalization uncertainties due to luminosity and cross section, jet energy correction uncertainties, and all uncertainties that are evaluated from event-based weights. A large part of the depicted uncertainties on the expected event yields are correlated. The lower panels show the ratio of data to the prediction. A value of $m_{t}^{\text{gen}} = 172.5\,\text{GeV}$ is used in the simulation.

of the mass extraction method. In the new profile likelihood approach, the statistical uncertainty in the top quark mass dependence due to the limited sample size is included via nuisance parameters.

- *Jet energy correction* (JEC)*:* Jet energies are scaled up and down according to the p_{T}- and η-dependent data/simulation uncertainties [24]. Each of the 25 individual uncertainties in the jet energy corrections is represented by its own nuisance parameter.
- *Jet energy resolution* (JER)*:* Since the JER measured in data is worse than in simulation, the simulation is modified to correct for the difference [24]. The jet energy resolution in the simulation is varied up and down within the uncertainty. The variation is evaluated independently for two $|\eta_{\text{jet}}|$ regions, split at $|\eta_{\text{jet}}| = 1.93$.
- *b tagging:* The p_{T}-dependent uncertainty of the b-tagging efficiencies and misidentification rates of the DEEPJET tagger [17, 26] are taken into account by reweighting the simulated events accordingly.
- *Pileup:* To estimate the uncertainty from the determination of the number of pileup events and the reweighting procedure, the inelastic pp cross section [55] used in the determination is varied by $\pm 4.6\%$.
- *Background* (BG)*:* The main uncertainty in the background stems from the uncertainty in the measurements of the cross sections used in the normalization. The normalization of the background samples is varied by $\pm 10\%$ for the single top quark samples [56, 57], $\pm 30\%$ for the W+jets samples [58], $\pm 10\%$ for the Z+jets [59] and for the diboson samples [60, 61], and $\pm 100\%$ for the QCD multijet samples. The size of the variations is the same as in the previous measurement [13] in this channel. The uncertainty in the luminosity of 1.2% [31] is negligible compared to these variations.
- *Lepton scale factors* (SFs) *and momentum scale:* The simulation-to-data scale factors for the trigger, reconstruction, and selection efficiencies for electrons and muons are varied within their uncertainties. In addition, the lepton energy in simulation is

varied up and down within its uncertainty.

- *JEC flavor:* The difference between Lund string fragmentation and cluster fragmentation is evaluated by comparing PYTHIA 6.422 [62] and HERWIG++ 2.4 [63]. The jet energy response is compared separately for each jet flavor [24].
- *b-jet modeling* (bJES)*:* The uncertainty associated with the fragmentation of b quarks is split into four components. The Bowler–Lund fragmentation function is varied symmetrically within its uncertainties, as determined by the ALEPH and DELPHI Collaborations [64, 65]. The difference between the default PYTHIA setting and the center of the variations is included as an additional uncertainty. As an alternative model of the fragmentation into b hadrons, the Peterson fragmentation function is used and the difference obtained relative to the Bowler–Lund fragmentation function is assigned as an uncertainty. The third uncertainty source taken into account is the semileptonic b-hadron branching fraction, which is varied by -0.45 and $+0.77\%$, motivated by measurements of $\mathrm{B}^0/\mathrm{B}^+$ decays and their corresponding uncertainties [8].
- *PDF:* The default PDF set in the simulation, NNPDF3.1 NNLO [37, 38], is replaced with the CT14 NNLO [66] and MMHT 2014 NNLO [67] PDFs via event weights. In addition, the default set is varied with 100 Hessian eigenvectors [38] and the α_S value is changed to 0.117 and 0.119. All described variations are evaluated for their impact on the measurement and the negligible variations are later omitted to reduce the number of nuisance parameters.
- *Renormalization and factorization scales:* The renormalization and factorization scales for the ME calculation are varied independently and simultaneously by factors of 2 and 1/2. This is achieved by reweighting the simulated events. The independent variations were checked and it was found to be sufficient to include only the simultaneous variations as a nuisance parameter.
- *ME to PS matching:* The matching of the POWHEG ME calculations to the PYTHIA PS is varied by shifting the parameter $h_\mathrm{damp} = 1.58^{+0.66}_{-0.59}$ [68] within its uncertainty.
- *ISR and FSR:* For initial-state radiation (ISR) and final-state radiation (FSR), 32 decorrelated variations of the renormalization scale and nonsingular terms for each branching type ($\mathrm{g} \to \mathrm{gg}$, $\mathrm{g} \to \mathrm{q\overline{q}}$, $\mathrm{q} \to \mathrm{qg}$, and $\mathrm{X} \to \mathrm{Xg}$ with $\mathrm{X} = \mathrm{t}$ or b) are applied using event weights [69]. The scale variations correspond to a change of the respective PS scale in PYTHIA by factors of 2 and 1/2. This approach is new compared to the previous analysis [13], which only evaluated correlated changes in the FSR and ISR PS scales.
- *Top quark* p_T*:* Recent calculations suggest that the top quark p_T spectrum is strongly affected by NNLO effects [70–72]. The p_T of the top quark in simulation is varied to match the distribution measured by CMS [73, 74]. The default simulation is not corrected for this effect, but this variation is included via a nuisance parameter in the m_t measurement.
- *Underlying event:* Measurements of the underlying event have been used to tune PYTHIA parameters describing nonperturbative QCD effects [16, 44]. The parameters of the tune are varied within their uncertainties.
- *Early resonance decays:* Modeling of color reconnection introduces systematic uncertainties, which are estimated by comparing different CR models and settings. In the default sample, the top quark decay products are not included in the CR process. This setting is compared to the case of including the decay products by enabling

early resonance decays in PYTHIA8.

- *CR modeling:* In addition to the default model used in PYTHIA8, two alternative CR models are used, namely a model with string formation beyond leading color ("QCD inspired") [75] and a model allowing the gluons to be moved to another string ("gluon move") [76]. Underlying event measurements are used to tune the parameters of all models [77]. For each model, an individual nuisance parameter is introduced.

5 Mass extraction method

A maximum likelihood (ML) fit to the selected events is employed to measure m_{t}. The evaluated likelihood ratio $\lambda(m_{\mathrm{t}}, \vec{\theta}, \vec{\beta}, \vec{\omega}|\mathrm{data})$ depends not only on m_{t}, but also on three sets of nuisance parameters. The nuisance parameters, $\vec{\theta}$, incorporate the uncertainty in systematic effects, while the statistical nuisance parameters, $\vec{\beta}$ and $\vec{\omega}$, account for the statistical uncertainties in the default simulation and in the simulation of variations of m_{t} or of the uncertainty sources. All nuisance parameters are normalized such that a value of 0 represents the absence of the systematic effect and the values ± 1 correspond to a variation of the systematic effect by one standard deviation up or down. The ROOFIT [78] package is used to define and evaluate all the functions. The minimum of the negative log-likelihood $-2 \ln \lambda(m_{\mathrm{t}}, \vec{\theta}, \vec{\beta}, \vec{\omega}|\mathrm{data})$ is found with the MINUIT2 package [79].

The data are characterized by the five observables per event mentioned in Section 4. The events are split into the electron+jets and the muon+jets channels. The input to the ML fit is a set of one-dimensional histograms of the observables, x_i, in the two P_{gof} categories. For each histogram, a suitable probability density function $P(x_i|m_{\mathrm{t}}, \vec{\theta}, \vec{\beta}, \vec{\omega})$ is derived from simulation.

The probability density function for the $m_{\mathrm{t}}^{\mathrm{fit}}$ histograms is approximated by the sum of a Voigt profile (the convolution of a Cauchy–Lorentz distribution and a Gaussian distribution) for the correctly reconstructed $\mathrm{t\bar{t}}$ candidates and Chebyshev polynomials for the remaining events. For all other observables, a binned probability density function is used that returns the relative fraction of events per histogram bin. Here, eight bins are used for each observable and the width of the bins is chosen so that each bin has a similar number of selected events for the default simulation ($m_{\mathrm{t}}^{\mathrm{gen}} = 172.5\,\mathrm{GeV}$). For the following, we denote the parameters of the probability density functions as $\vec{\alpha}$. All the functions $P_i(x_i|\vec{\alpha})$ are normalized to the number of events in the histogram for the observable x_i, so only shape information is used in the ML fit. Hence, the parameters $\vec{\alpha}$ are correlated even for the binned probability density function. The dependence of these parameters on m_{t} and $\vec{\theta}$ is assumed to be linear. The full expression is for a component α_k of $\vec{\alpha}$

$$\alpha_k = C_k \left(1 + d_k \left[\alpha_k^0 + \beta_k + s_k^0 \, (m_{\mathrm{t}} - 172.5\,\mathrm{GeV}) + \omega_k^0 \, 1\,\mathrm{GeV}\right]\right) \prod_l \left(1 + d_k \left[s_k^l \, \theta_l + \omega_k^l \, 1\right]\right),$$

with k indicating the parameter of the probability density function for the observable and l indicating the nuisance parameter. For the nuisance parameters corresponding to the FSR PS scale variations, the linear term, $s_k^l \, \theta_l$, is replaced with a second-order polynomial. With this substitution, the probability density function, $P_i(x_i|\vec{\alpha})$, for an observable x_i becomes the function $P_i(x_i|m_{\mathrm{t}}, \vec{\theta}, \vec{\beta}, \vec{\omega})$ mentioned above.

The model parameter α_k^0 is determined by a fit to the default simulation, while the linear dependencies of α_k on m_{t} or a component θ_l of $\vec{\theta}$ are expressed with the model parameters s_k^0 and

s_k^l, respectively. The parameter s_k^0 is determined from a simultaneous fit to simulated samples, where m_t^{gen} is varied by ± 3 GeV from the default value. Along the same lines, the parameters s_k^l are obtained from fits to the simulation of the systematic effect corresponding to the nuisance parameter θ_l. The values of C_k and d_k are chosen ad hoc so that the results of the fits of a_k^0, s_k^0, and the s_k^l are all of the same order of magnitude and with a similar statistical uncertainty. This improves the numerical stability of the final ML fit.

The limited size of the simulated samples for different m_t^{gen} values gives rise to a calibration uncertainty in m_t. Hence, additional statistical nuisance parameters, β_k and ω_k^0, are introduced that account for the statistical uncertainty in the model parameters a_k^0 and s_k^0, similar to the Barlow–Beeston approach [80, 81]. The size of the statistical uncertainty in the m_t dependence, s_k^0, is scaled down, as we expect the measured m_t value to fall into an interval around the default value corresponding to a standard deviation of ± 1 GeV. Similarly, the parameters s_k^l contain random fluctuations if they are determined from simulated samples that are statistically independent to the default simulation and of limited size. These fluctuations can lead to overconstraints on the corresponding nuisance parameters and, hence, an underestimation of the systematic uncertainty. The nuisance parameters ω_k^l are added to counter these effects.

For a single histogram in a set, the products of Poisson probabilities for the prediction $\mu_{i,j} = n_{tot,i} P_i(x_{i,j}|m_t, \vec{\theta}, \vec{\beta}, \vec{\omega})$ and for an alternative model with an adjustable parameter per bin $\hat{\mu}_{i,j} = n_{i,j}$ are used to compute the likelihood ratio λ_i [8], where x_i is the observable, $n_{i,j}$ is the content of bin j with bin center $x_{i,j}$, and $n_{tot,i}$ is the total number of entries. Then the combined likelihood ratio for a set with observables $\vec{x}$ is

$$\lambda(m_t, \vec{\theta}, \vec{\beta}, \vec{\omega}|\text{data}) = \left(\prod_i \lambda_i(m_t, \vec{\theta}, \vec{\beta}, \vec{\omega}|x_i) P(\vec{\beta}) P(\vec{\omega}) \right) \left(\prod_l P(\theta_l) \right),$$

where $P(\theta_l)$, $P(\vec{\beta})$, and $P(\vec{\omega})$ are the pre-fit probability density functions of the nuisance parameters θ_l, $\vec{\beta}$, and $\vec{\omega}$. The product of the likelihood ratios can be used on the right-hand side of the equation, as all observables are independent in most phase space regions. The probability density functions of the nuisance parameters related to the sources of systematic uncertainties, $P(\theta_l)$, are standard normal distributions. The statistical nuisance parameters $\vec{\beta}$ and $\vec{\omega}$ are constrained by centered multivariate normal distributions, where their covariance matrices are taken from the fit of the model parameters. The latter nuisance parameters and constraints are only included if the model parameters are determined from samples that are statistically independent of the default simulation, like, for example, for the alternative color reconnection models. If the model parameters are determined from samples obtained from varying the default simulation with event-based weights or scaling or smearing of the jet energies, the corresponding ω parameters are fixed to zero and the constraint is removed from $\lambda(m_t, \vec{\theta}, \vec{\beta}, \vec{\omega}|\text{data})$.

The mass of the top quark is determined with the profile likelihood fit for different sets of data histograms. The sets and their labels are listed in Table 1.

The expected total uncertainty in m_t is evaluated for each set defined in Table 1 with pseudo-experiments using the default simulation. The results of the pseudo-experiments are shown in Fig. 4 (left). The improvements in the data reconstruction and calibration, event selection, simulation, and mass extraction method reduce the uncertainty in the *1D* measurement from 1.09 to 0.63 GeV, when compared to the previous measurement [13]. The uncertainty in the *2D* measurement improves from 0.63 to 0.50 GeV. The additional observables and the split into categories further reduce the expected uncertainty down to 0.37 GeV for the *5D* set.

Table 1: The overall list of different input histograms and their inclusion in a certain histogram set. A histogram marked with "×" is included in a set (measurement).

Histogram		Set label				
Observable	Category	*1D*	*2D*	*3D*	*4D*	*5D*
$m_{\mathrm{t}}^{\mathrm{fit}}$	$P_{\mathrm{gof}} > 0.2$	×	×	×	×	×
$m_{\mathrm{W}}^{\mathrm{reco}}$	$P_{\mathrm{gof}} > 0.2$		×	×	×	×
$m_{\ell\mathrm{b}}^{\mathrm{reco}}$	$P_{\mathrm{gof}} < 0.2$			×	×	×
$m_{\ell\mathrm{b}}^{\mathrm{reco}} / m_{\mathrm{t}}^{\mathrm{fit}}$	$P_{\mathrm{gof}} > 0.2$				×	×
$R_{\mathrm{bq}}^{\mathrm{reco}}$	$P_{\mathrm{gof}} > 0.2$					×

The statistical uncertainty is obtained from fits that only have m_{t} as a free parameter. From studies on simulation, it is expected to be 0.07, 0.06, and 0.04 GeV in the electron+jets, muon+jets, and the combined (lepton+jets) channels, respectively.

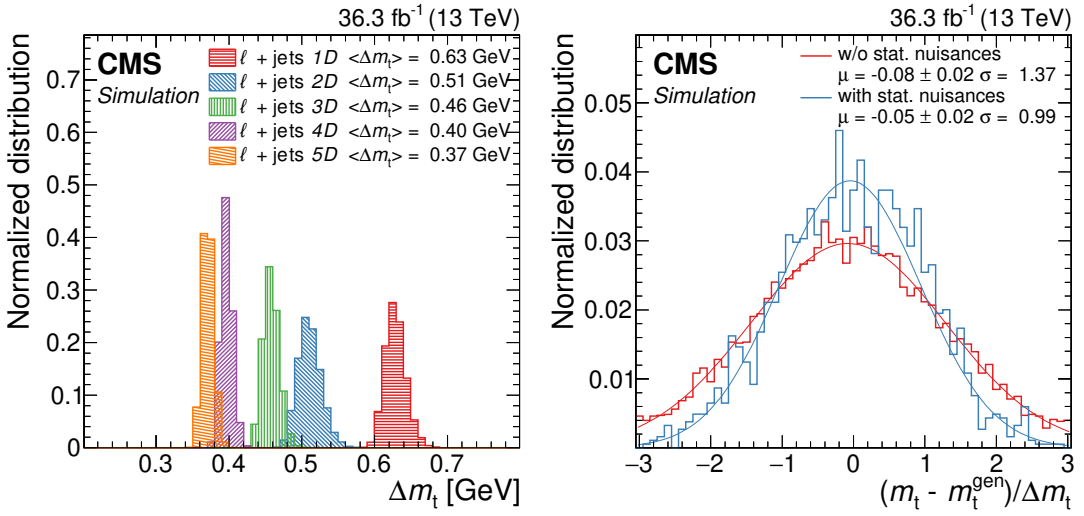

Figure 4: Left: Comparison of the expected total uncertainty in m_{t} in the combined lepton+jets channel and for the different observable-category sets defined in Table 1. Right: The difference between the measured and generated m_{t} values, divided by the uncertainty reported by the fit from pseudo-experiments without (red) or with (blue) the statistical nuisance parameters $\vec{\beta}$ and $\vec{\omega}$ in the *5D* ML fit. Also included in the legend are the μ and σ parameters of Gaussian functions (red and blue lines) fit to the histograms.

The applied statistical model is verified with additional pseudo-experiments. Here, the data for one pseudo-experiment are generated using probability density functions $P(x_i|m_{\mathrm{t}}, \vec{\theta})$ that have the same functional form as the ones used in the ML fit, but their model parameters $\vec{\alpha}$ and $\vec{s}$ are determined on statistically fluctuated simulations. For the generation of a pseudo-experiment, m_{t} is chosen from a uniform distribution with a mean of 172.5 GeV and the same standard deviation as is assumed for the calibration uncertainty. The values of the nuisance parameters $\vec{\theta}$ are drawn from standard normal distributions. The same ML fit that is applied to the collider data is then performed on the pseudo-data. The pseudo-experiments are generated for two cases, specifically, with and without the statistical nuisance parameters $\vec{\beta}$ and $\vec{\omega}$ in the ML fit. Figure 4 (right) shows the distribution of the differences between the measured and generated m_{t} values, divided by the uncertainty reported by the fit for both cases. A nearly 40% underestimation of the measurement uncertainty can be seen for the case without the statistical nuisance parameters $\vec{\beta}$ and $\vec{\omega}$, while consistency is observed for the method that is

employed on data.

In addition, single-parameter fits were performed on pseudo-data sampled from simulation to verify that the mass extraction method is unbiased and reports the correct uncertainty. These tests were done for fits of m_t with samples corresponding to mass values of 169.5, 172.5, and 175.5 GeV, as well as on the simulation of different systematic effects for the fits of the corresponding nuisance parameter.

6 Results

The results of the profile likelihood fits to data are shown in Fig. 5 for the electron+jets, muon+jets, and lepton+jets channels and for the different sets of observables and categories, as defined in Table 1. The observables m_W^{reco}, $m_{\ell b}^{reco}/m_t^{fit}$, and R_{bq}^{reco} provide constraints on the modeling of the $t\bar{t}$ decays in addition to the observables m_t^{fit} and $m_{\ell b}^{reco}|_{P_{gof}<0.2}$, which are highly sensitive to m_t. With the profile likelihood method, these constraints not only reduce the uncertainty in m_t, but also change the measured m_t value, as they effectively alter the parameters of the reference $t\bar{t}$ simulation. When additional observables are included, the measurement in the lepton+jets channel yields a smaller mass value than the single-lepton channels because of the correlations between the channels.

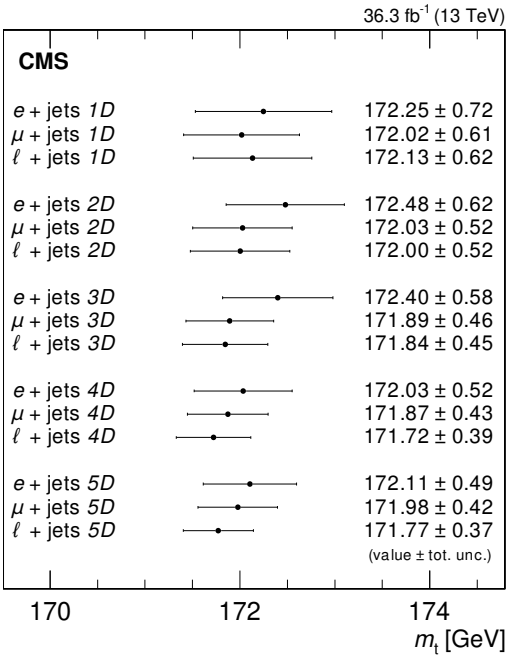

Figure 5: Measurement of m_t in the three different channels for the different sets of observables and categories as defined in Table 1.

The *5D* fit to the selected events results in the best precision and yields in the respective channels:

$$\begin{aligned} \text{Electron+jets:} \quad m_t^{5D} &= 172.11 \pm 0.49\,\text{GeV}, \\ \text{Muon+jets:} \quad m_t^{5D} &= 171.98 \pm 0.42\,\text{GeV}, \\ \text{Lepton+jets:} \quad m_t^{5D} &= 171.77 \pm 0.37\,\text{GeV}. \end{aligned}$$

The comparisons of the data distributions and the post-fit *5D* model are shown in Fig. 6.

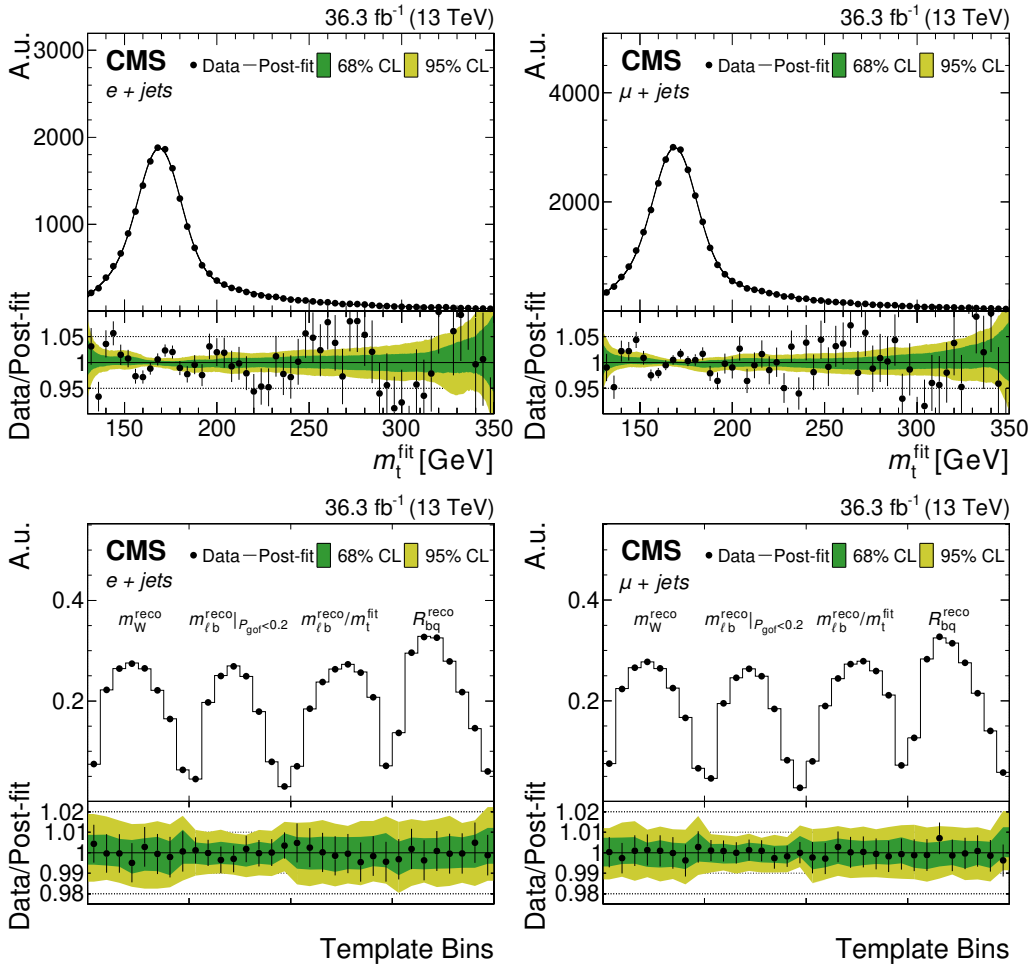

Figure 6: Distribution of m_t^{fit} (upper) and the additional observables (lower) that are the input to the *5D* ML fit and their post-fit probability density functions for the combined fit to the electron+jets (left) and muon+jets (right) channels. The lower panels show the ratio of data and post-fit template values. The green and yellow bands represent the 68 and 95% confidence levels in the fit uncertainty.

Figure 7 shows the pulls on the most important systematic nuisance parameters θ and their impacts on m_t, Δm_t, after the fit with the *5D* model. The pulls are defined as $(\hat{\theta} - \theta_0)/\Delta\theta$, where $\hat{\theta}$ is the measured nuisance parameter value and θ_0 and $\Delta\theta$ are the mean and standard deviation of the nuisance parameter before the fit. The post-fit impacts are evaluated by repeating the ML fit with the studied nuisance parameter θ fixed to $\hat{\theta} \pm \widehat{\Delta\theta}$, where $\widehat{\Delta\theta}$ is the uncertainty in the nuisance parameter after the fit. The pre-fit impacts are evaluated with $\hat{\theta}$ and $\Delta\theta$, respectively. If the systematic nuisance parameters θ have statistical nuisance parameters ω that account for the statistical uncertainty in the θ-dependence of the model, the corresponding statistical nuisance parameters ω are fixed to their post-fit values in the impact evaluation. In this case, the post-fit impact plotted in Fig. 7 is the combined impact of the systematic and statistical nuisance parameters. To estimate the combined impact, the likelihood fit is repeated with the corresponding nuisance parameters fixed to their post-fit values and the quadratic difference of the overall m_t uncertainty compared to the default fit is taken. The quadratic difference between the combined impact and the post-fit impact of only the systematic nuisance parameter is interpreted as the effect of the limited size of the systematic simulation samples.

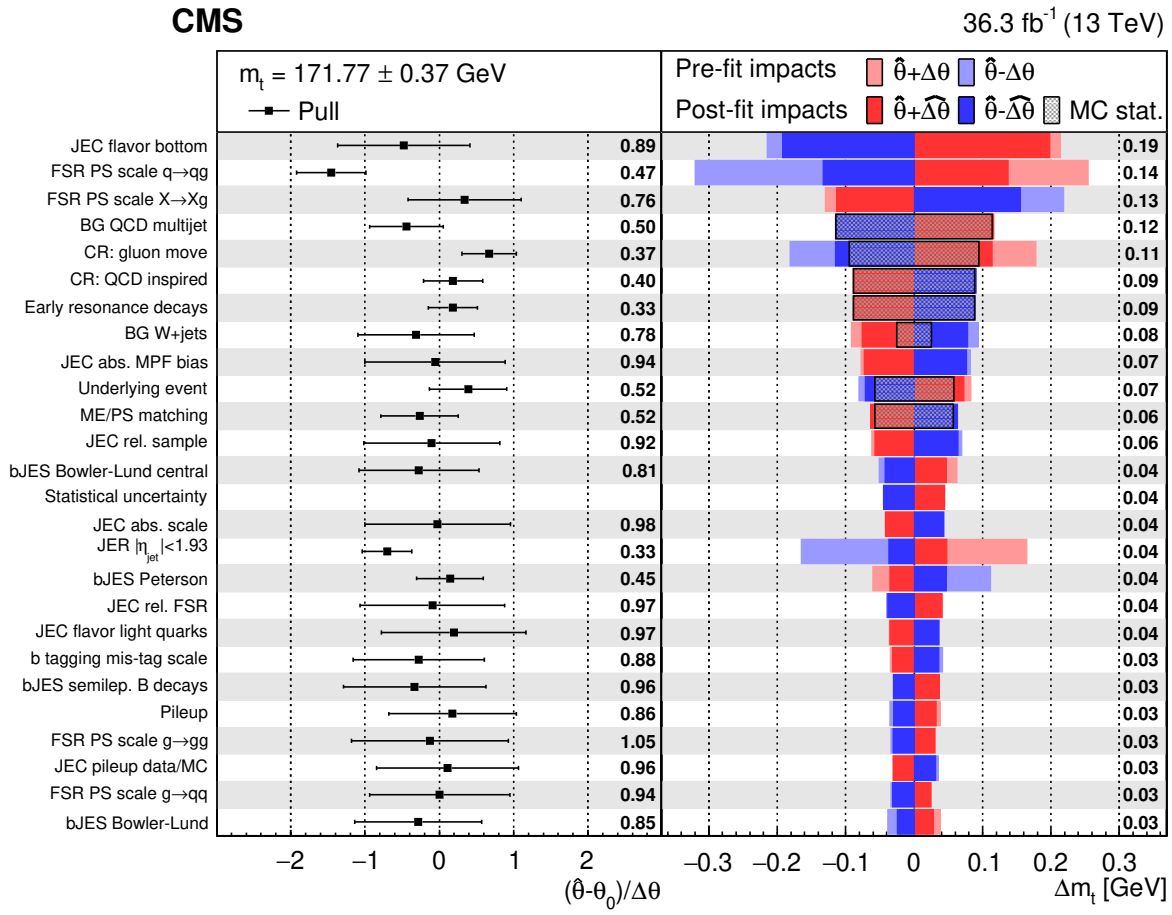

Figure 7: Measurement of m_t in the combined lepton+jets channel using the *5D* set of observables and categories. The left plot shows the post-fit pulls on the most important nuisance parameters and the numbers quote the post-fit uncertainty in the nuisance parameter. The right plot shows their pre-fit (lighter colored bars) and post-fit impacts (darker colored bars) on m_t for up (red) and down (blue) variations. The post-fit impacts include the contribution from the nuisance parameters accounting for the limited size of simulation samples (MC stat. as gray-dotted areas). The average of the post-fit impacts for up and down variations is printed on the right. The rows are sorted by the size of the averaged post-fit impact. The statistical uncertainty in m_t is depicted in the corresponding row.

Most nuisance parameters are consistent with their pre-fit values. Many of the nuisance parameters that show a strong post-fit constraint correspond to systematic uncertainties that are evaluated on independent samples of limited size and are accompanied by additional statistical nuisance parameters. A comparison of the pre-fit and post-fit impacts where the post-fit impacts include the impact of these statistical nuisance parameters shows that there is an only minimal constraint by the fit on the corresponding systematic uncertainties. In addition, the impact of the JER uncertainty is strongly reduced by the fit, as the energy resolution of jets from $\mathrm{t\bar{t}}$ decays can be measured much better from the width of the m_W^{reco} distribution than by the extrapolation of the resolution measurement with dijet topologies at much higher transverse momenta [24].

None of the nuisance parameters have a statistically significant deviation from zero after the fit. The largest effect on the measured mass value corresponds to the FSR scale of the $q \to qg$ branching type. The effect is caused by the difference in the peak position of m_W^{reco} seen in

Fig. 2 (left). The previous measurements in this channel by the CMS Collaboration assumed correlated FSR PS scales with the same scale choice for jets induced by light quarks and b quarks [11, 13]. In that case, a lower peak position in the $m_{\mathrm{W}}^{\mathrm{reco}}$ distribution would also cause the $m_{\mathrm{t}}^{\mathrm{fit}}$ peak position to be lower than expected from simulation for a given m_{t} value, resulting in a higher top quark mass value to be measured. In fact, a *5D* fit to data assuming fully correlated FSR PS scale choices yields $m_{\mathrm{t}} = 172.20 \pm 0.31\,\mathrm{GeV}$. This value is very close to the previous measurement on the same data of $m_{\mathrm{t}} = 172.25 \pm 0.63\,\mathrm{GeV}$ [13]. The measurement is repeated for different correlation coefficients (ρ_{FSR}) in the pre-fit covariance matrix between the FSR PS scales for the different branching types. The result of this study is shown in Fig. 8. The final result strongly depends on the choice of the correlation coefficient between the FSR PS scales because of the significant deviation for the FSR PS scale of the $\mathrm{q} \to \mathrm{qg}$ branching from the default simulation. However, the assumption of strongly correlated FSR PS scale choices would also significantly reduce the overall uncertainty, as the impacts from the scale choice for gluon radiation from b quarks ($\mathrm{X} \to \mathrm{Xg}$) and light quarks ($\mathrm{q} \to \mathrm{qg}$) partially cancel. In addition, there is a tension between the measured nuisance parameter values for the different FSR PS scales which disfavors a strong correlation. As there is only a small dependence on FSR PS scale correlations at low correlation coefficients ($\rho_{\mathrm{FSR}} < 0.5$), and uncorrelated nuisance parameters for the FSR PS scales receive the least constraint from the fit to data, we assume uncorrelated FSR PS scales for this measurement.

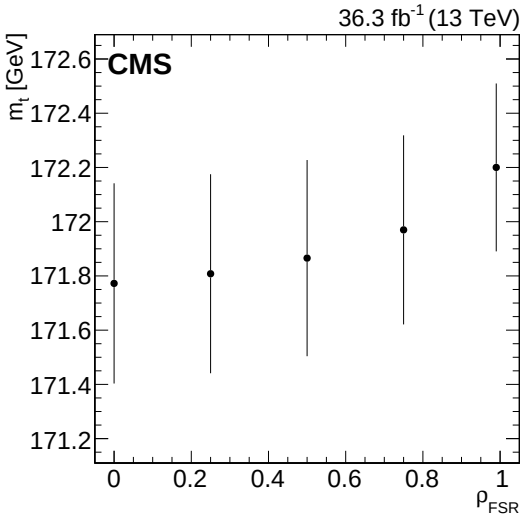

Figure 8: Dependence of the *5D* result on the assumed correlation ρ_{FSR} between the FSR PS scales in the lepton+jets channel.

Table 2 compares the measurements by the *2D* and *5D* methods with the previous result [13] for the same data-taking period. The JEC uncertainties are grouped following the recommendations documented in Ref. [82]. The uncertainty in m_{t} for one source (row) in this table is evaluated from the covariance matrix of the ML fit by taking the square root of $\mathrm{cov}(m_{\mathrm{t}}, X)\mathrm{cov}(X, X)^{-1}\mathrm{cov}(X, m_{\mathrm{t}})$, where $\mathrm{cov}(m_{\mathrm{t}}, X)$, $\mathrm{cov}(X, X)$, $\mathrm{cov}(X, m_{\mathrm{t}})$ are the parts of the covariance matrix related to m_{t} or the set of nuisance parameters X contributing to the source, respectively. The statistical and calibration uncertainties are obtained differently by computing the partial covariance matrix on m_{t} where all other nuisance parameters are removed. The quadratic sum of all computed systematic uncertainties is larger than the uncertainty in m_{t} from the ML fit, as the sum ignores the post-fit correlations between the systematic uncertainty sources.

The *5D* method is the only method that surpasses the strong reduction in the uncertainty in

Table 2: Comparison of the uncertainty in the top quark mass in the previous measurement [13] and the new *2D* and *5D* results in the lepton+jets channel.

	δm_t [GeV]		
	previous *2D*	*2D*	*5D*
Experimental uncertainties			
Method calibration	0.05	0.02	0.02
JEC	0.18	0.32	0.16
– Intercalibration	0.04	0.10	0.04
– MPFInSitu	0.07	0.15	0.07
– Uncorrelated	0.16	0.21	0.10
Jet energy resolution	0.12	0.12	0.05
b tagging	0.03	0.01	0.03
Lepton SFs and mom. scale		0.00	0.03
Pileup	0.05	0.00	0.03
Background	0.02	0.12	0.15
Modeling uncertainties			
JEC flavor	0.39	0.30	0.20
b-jet modeling	0.12	0.15	0.11
PDF	0.02	0.00	0.01
Ren. and fact. scales	0.01	0.03	0.02
ME/PS matching	0.07	0.06	0.07
ISR PS scale	0.07	0.01	0.01
FSR PS scale	0.13	0.37	0.21
Top quark p_T	0.01	0.06	0.00
Underlying event	0.07	0.09	0.04
Early resonance decays	0.07	0.13	0.09
CR modeling	0.31	0.15	0.15
Statistical	0.08	0.05	0.04
Total	0.63	0.52	0.37

the JEC achieved by the previous analysis that determined m_t and in situ an overall jet energy scale factor (JSF). However, the measurement presented here also constrains the jet energy resolution uncertainty that was unaffected by the JSF. The new observables and additional events with a low P_{gof} reduce most modeling uncertainties, but lead to a slight increase in some experimental uncertainties. While the usage of weights for the PS variations removes the previously significant statistical component in the PS uncertainties, the introduction of separate PS scales leads to a large increase in the uncertainty in the FSR PS scale, despite the tight constraint on the corresponding nuisance parameters shown in Fig. 7.

The result presented here achieves a considerable improvement compared to all previously published top quark mass measurements. Hence, it supersedes the previously published measurement in this channel on the same data set [13]. The analysis shows the precision that is achievable from direct measurements of the top quark mass. As the uncertainty in the relationship of the direct measurement from simulation templates to a theoretically well-defined top quark mass is currently of similar size, the measurement should fuel further theoretical studies on the topic.

7 Summary

The mass of the top quark is measured using LHC proton-proton collision data collected in 2016 with the CMS detector at $\sqrt{s} = 13\,\text{TeV}$, corresponding to an integrated luminosity of $36.3\,\text{fb}^{-1}$. The measurement uses a sample of $\mathrm{t\bar{t}}$ events containing one isolated electron or muon and at least four jets in the final state. For each event, the mass is reconstructed from a kinematic fit of the decay products to a $\mathrm{t\bar{t}}$ hypothesis. A likelihood method is applied using up to five observables to extract the top quark mass and constrain the influences of systematic effects, which are included as nuisance parameters in the likelihood. The top quark mass is measured to be $171.77 \pm 0.37\,\text{GeV}$. This result achieves a considerable improvement compared to all previously published top quark mass measurements and supersedes the previously published measurement in this channel on the same data set.

References

[1] CDF Collaboration, "Observation of top quark production in $\bar{p}p$ collisions", *Phys. Rev. Lett.* **74** (1995) 2626, doi:10.1103/PhysRevLett.74.2626, arXiv:hep-ex/9503002.

[2] D0 Collaboration, "Observation of the top quark", *Phys. Rev. Lett.* **74** (1995) 2632, doi:10.1103/PhysRevLett.74.2632, arXiv:hep-ex/9503003.

[3] G. Degrassi et al., "Higgs mass and vacuum stability in the standard model at NNLO", *JHEP* **08** (2012) 1, doi:10.1007/JHEP08(2012)098, arXiv:1205.6497.

[4] F. Bezrukov, M. Y. Kalmykov, B. A. Kniehl, and M. Shaposhnikov, "Higgs boson mass and new physics", *JHEP* **10** (2012) 140, doi:10.1007/JHEP10(2012)140, arXiv:1205.2893.

[5] The ALEPH, DELPHI, L3, and OPAL Collaborations and the LEP Electroweak Working Group, "Electroweak measurements in electron-positron collisions at W-boson-pair energies at LEP", *Phys. Rept.* **532** (2013) 119, doi:10.1016/j.physrep.2013.07.004, arXiv:1302.3415.

[6] M. Baak et al., "The electroweak fit of the standard model after the discovery of a new boson at the LHC", *Eur. Phys. J. C* **72** (2012) 2205, doi:10.1140/epjc/s10052-012-2205-9, arXiv:1209.2716.

[7] M. Baak et al., "The global electroweak fit at NNLO and prospects for the LHC and ILC", *Eur. Phys. J. C* **74** (2014) 3046, doi:10.1140/epjc/s10052-014-3046-5, arXiv:1407.3792.

[8] Particle Data Group, P. A. Zyla et al., "Review of particle physics", *Prog. Theor. Exp. Phys.* **2020** (2020) 083C01, doi:10.1093/ptep/ptaa104.

[9] CDF and D0 Collaborations, "Combination of CDF and D0 results on the mass of the top quark using up $9.7\,\text{fb}^{-1}$ at the Tevatron", FERMILAB-CONF-16-298-E, 2016. arXiv:1608.01881.

[10] ATLAS Collaboration, "Measurement of the top quark mass in the $t\bar{t} \to$ lepton+jets channel from $\sqrt{s} = 8$ TeV ATLAS data and combination with previous results", *Eur. Phys. J. C* **79** (2019) 290, doi:10.1140/epjc/s10052-019-6757-9, arXiv:1810.01772.

[11] CMS Collaboration, "Measurement of the top quark mass using proton-proton data at $\sqrt{s}$ = 7 and 8 TeV", *Phys. Rev. D* **93** (2016) 072004, doi:10.1103/PhysRevD.93.072004, arXiv:1509.04044.

[12] A. H. Hoang, "What is the top quark mass?", *Ann. Rev. Nucl. Part. Sci.* **70** (2020) 225, doi:10.1146/annurev-nucl-101918-023530, arXiv:2004.12915.

[13] CMS Collaboration, "Measurement of the top quark mass with lepton+jets final states using pp collisions at $\sqrt{s} = 13$ TeV", *Eur. Phys. J. C* **78** (2018) 891, doi:10.1140/epjc/s10052-018-6332-9, arXiv:1805.01428.

[14] DELPHI Collaboration, "Measurement of the mass and width of the W boson in e^+e^- collisions at $\sqrt{s}$ = 161–209 GeV", *Eur. Phys. J. C* **55** (2008) 1, doi:10.1140/epjc/s10052-008-0585-7, arXiv:0803.2534.

[15] CMS Collaboration, "Measurement of the top-quark mass in $t\bar{t}$ events with lepton+jets final states in pp collisions at $\sqrt{s} = 7$ TeV", *JHEP* **12** (2012) 105, doi:10.1007/JHEP12(2012)105, arXiv:1209.2319.

[16] CMS Collaboration, "Extraction and validation of a new set of CMS PYTHIA8 tunes from underlying-event measurements", *Eur. Phys. J. C* **80** (2020) 4, doi:10.1140/epjc/s10052-019-7499-4, arXiv:1903.12179.

[17] E. Bols et al., "Jet flavour classification using DeepJet", *JINST* **15** (2020) P12012, doi:10.1088/1748-0221/15/12/P12012, arXiv:2008.10519.

[18] HEPData record for this analysis, 2022. doi:10.17182/hepdata.127993.

[19] CMS Collaboration, "The CMS experiment at the CERN LHC", *JINST* **3** (2008) S08004, doi:10.1088/1748-0221/3/08/S08004.

[20] CMS Collaboration, "Technical proposal for the Phase-II upgrade of the Compact Muon Solenoid", CMS Technical Proposal CERN-LHCC-2015-010, CMS-TDR-15-02, 2015.

[21] CMS Collaboration, "Particle-flow reconstruction and global event description with the CMS detector", *JINST* **12** (2017) P10003, doi:10.1088/1748-0221/12/10/P10003, arXiv:1706.04965.

[22] M. Cacciari, G. P. Salam, and G. Soyez, "The anti-k_T jet clustering algorithm", *JHEP* **04** (2008) 063, doi:10.1088/1126-6708/2008/04/063, arXiv:0802.1189.

[23] M. Cacciari, G. P. Salam, and G. Soyez, "FastJet user manual", *Eur. Phys. J. C* **72** (2012) 1896, doi:10.1140/epjc/s10052-012-1896-2, arXiv:1111.6097.

[24] CMS Collaboration, "Jet energy scale and resolution in the CMS experiment in pp collisions at 8 TeV", *JINST* **12** (2017) P02014, doi:10.1088/1748-0221/12/02/P02014, arXiv:1607.03663.

[25] CMS Collaboration, "Identification of heavy-flavour jets with the CMS detector in pp collisions at 13 TeV", 2017. arXiv:1712.07158. Submitted to *JINST*.

[26] CMS Collaboration, "Performance of the DeepJet b tagging algorithm using 41.9/fb of data from proton-proton collisions at 13 TeV with Phase 1 CMS detector", CMS Detector Performance Note CMS-DP-2018-058, 2018.

[27] CMS Collaboration, "Performance of missing transverse momentum reconstruction in proton-proton collisions at $\sqrt{s} = 13$ TeV using the CMS detector", *JINST* **14** (2019) P07004, doi:10.1088/1748-0221/14/07/P07004, arXiv:1903.06078.

[28] CMS Collaboration, "Electron and photon reconstruction and identification with the CMS experiment at the CERN LHC", *JINST* **16** (2021) P05014, doi:10.1088/1748-0221/16/05/P05014, arXiv:2012.06888.

[29] CMS Collaboration, "ECAL 2016 refined calibration and Run2 summary plots", CMS Detector Performance Note CMS-DP-2020-021, 2020.

[30] CMS Collaboration, "Performance of the CMS muon detector and muon reconstruction with proton-proton collisions at $\sqrt{s} = 13$ TeV", *JINST* **13** (2018) P06015, doi:10.1088/1748-0221/13/06/P06015, arXiv:1804.04528.

[31] CMS Collaboration, "Precision luminosity measurement in proton-proton collisions at $\sqrt{s} = 13$ TeV in 2015 and 2016 at CMS", *Eur. Phys. J. C* **81** (2021) 800, doi:10.1140/epjc/s10052-021-09538-2, arXiv:2104.01927.

[32] CMS Collaboration, "The CMS trigger system", *JINST* **12** (2017) P01020, doi:10.1088/1748-0221/12/01/P01020, arXiv:1609.02366.

[33] P. Nason, "A new method for combining NLO QCD with shower Monte Carlo algorithms", *JHEP* **11** (2004) 040, doi:10.1088/1126-6708/2004/11/040, arXiv:hep-ph/0409146.

[34] S. Frixione, P. Nason, and C. Oleari, "Matching NLO QCD computations with parton shower simulations: the POWHEG method", *JHEP* **11** (2007) 070, doi:10.1088/1126-6708/2007/11/070, arXiv:0709.2092.

[35] S. Alioli, P. Nason, C. Oleari, and E. Re, "A general framework for implementing NLO calculations in shower Monte Carlo programs: the POWHEG BOX", *JHEP* **06** (2010) 043, doi:10.1007/JHEP06(2010)043, arXiv:1002.2581.

[36] T. Sjöstrand et al., "An introduction to PYTHIA8.2", *Comput. Phys. Commun.* **191** (2015) 159, doi:10.1016/j.cpc.2015.01.024, arXiv:1410.3012.

[37] J. Butterworth et al., "PDF4LHC recommendations for LHC Run II", *J. Phys. G* **43** (2016) 023001, doi:10.1088/0954-3899/43/2/023001, arXiv:1510.03865.

[38] NNPDF Collaboration, "Parton distributions from high-precision collider data", *Eur. Phys. J. C* **77** (2017) 663, doi:10.1140/epjc/s10052-017-5199-5, arXiv:1706.00428.

[39] S. Alioli, P. Nason, C. Oleari, and E. Re, "NLO single-top production matched with shower in POWHEG: s- and t-channel contributions", *JHEP* **09** (2009) 111, doi:10.1088/1126-6708/2009/09/111, arXiv:0907.4076. [Erratum: doi:10.1007/JHEP02(2010)011].

[40] E. Re, "Single-top Wt-channel production matched with parton showers using the POWHEG method", *Eur. Phys. J. C* **71** (2011) 1547, doi:10.1140/epjc/s10052-011-1547-z, arXiv:1009.2450.

[41] J. Alwall et al., "The automated computation of tree-level and next-to-leading order differential cross sections, and their matching to parton shower simulations", *JHEP* **07** (2014) 079, doi:10.1007/JHEP07(2014)079, arXiv:1405.0301.

[42] J. Alwall et al., "Comparative study of various algorithms for the merging of parton showers and matrix elements in hadronic collisions", *Eur. Phys. J. C* **53** (2008) 473, doi:10.1140/epjc/s10052-007-0490-5, arXiv:0706.2569.

[43] R. Frederix and S. Frixione, "Merging meets matching in MC@NLO", *JHEP* **12** (2012) 061, doi:10.1007/JHEP12(2012)061, arXiv:1209.6215.

[44] P. Skands, S. Carrazza, and J. Rojo, "Tuning PYTHIA8.1: the Monash 2013 tune", *Eur. Phys. J. C* **74** (2014) 3024, doi:10.1140/epjc/s10052-014-3024-y, arXiv:1404.5630.

[45] GEANT4 Collaboration, "GEANT4—a simulation toolkit", *Nucl. Instrum. Meth. A* **506** (2003) 250, doi:10.1016/S0168-9002(03)01368-8.

[46] M. Czakon and A. Mitov, "Top++: A program for the calculation of the top-pair cross-section at hadron colliders", *Comput. Phys. Commun.* **185** (2014) 2930, doi:10.1016/j.cpc.2014.06.021, arXiv:1112.5675.

[47] Y. Li and F. Petriello, "Combining QCD and electroweak corrections to dilepton production in FEWZ", *Phys. Rev. D* **86** (2012) 094034, doi:10.1103/PhysRevD.86.094034, arXiv:1208.5967.

[48] M. Aliev et al., "HATHOR: HAdronic Top and Heavy quarks crOss section calculatoR", *Comput. Phys. Commun.* **182** (2011) 1034, doi:10.1016/j.cpc.2010.12.040, arXiv:1007.1327.

[49] P. Kant et al., "HATHOR for single top-quark production: Updated predictions and uncertainty estimates for single top-quark production in hadronic collisions", *Comput. Phys. Commun.* **191** (2015) 74, doi:10.1016/j.cpc.2015.02.001, arXiv:1406.4403.

[50] D0 Collaboration, "Direct measurement of the top quark mass at D0", *Phys. Rev. D* **58** (1998) 052001, doi:10.1103/PhysRevD.58.052001, arXiv:hep-ex/9801025.

[51] ATLAS Collaboration, "Measurement of the top quark mass in the $t\bar{t} \to$ dilepton channel from $\sqrt{s} = 8$ TeV ATLAS data", *Phys. Lett. B* **761** (2016) 350, doi:10.1016/j.physletb.2016.08.042, arXiv:1606.02179.

[52] CMS Collaboration, "Measurement of the $t\bar{t}$ production cross section, the top quark mass, and the strong coupling constant using dilepton events in pp collisions at $\sqrt{s} = 13$ TeV", *Eur. Phys. J. C* **79** (2019) 368, doi:10.1140/epjc/s10052-019-6863-8, arXiv:1812.10505.

[53] ATLAS Collaboration, "Measurement of the top quark mass in the $t\bar{t} \to$ lepton+jets and $t\bar{t} \to$ dilepton channels using $\sqrt{s} = 7$ TeV ATLAS data", *Eur. Phys. J. C* **75** (2015) 330, doi:10.1140/epjc/s10052-015-3544-0, arXiv:1503.05427.

[54] CMS Collaboration, "Measurement of the top quark mass in the all-jets final state at $\sqrt{s} = 13$ TeV and combination with the lepton+jets channel", *Eur. Phys. J. C* **79** (2019) 313, doi:10.1140/epjc/s10052-019-6788-2, arXiv:1812.10534.

[55] CMS Collaboration, "Measurement of the inelastic proton-proton cross section at $\sqrt{s} = 13$ TeV", *JHEP* **07** (2018) 161, doi:10.1007/JHEP07(2018)161, arXiv:1802.02613.

[56] CMS Collaboration, "Measurement of the t-channel single-top-quark production cross section and of the $|V_{tb}|$ CKM matrix element in pp collisions at $\sqrt{s} = 8$ TeV", *JHEP* **06** (2014) 090, doi:10.1007/JHEP06(2014)090, arXiv:1403.7366.

[57] CMS Collaboration, "Cross section measurement of t-channel single top quark production in pp collisions at $\sqrt{s} = 13$ TeV", *Phys. Lett. B* **772** (2017) 752, doi:10.1016/j.physletb.2017.07.047, arXiv:1610.00678.

[58] CMS Collaboration, "Measurement of the production cross section of a W boson in association with two b jets in pp collisions at $\sqrt{s} = 8$ TeV", *Eur. Phys. J C.* **77** (2017) 92, doi:10.1140/epjc/s10052-016-4573-z, arXiv:1608.07561.

[59] CMS Collaboration, "Measurements of the associated production of a Z boson and b jets in pp collisions at $\sqrt{s} = 8$ TeV", *Eur. Phys. J. C* **77** (2017) 751, doi:10.1140/epjc/s10052-017-5140-y, arXiv:1611.06507.

[60] CMS Collaboration, "Measurement of the WZ production cross section in pp collisions at $\sqrt{s} = 13$ TeV", *Phys. Lett. B* **766** (2017) 268, doi:10.1016/j.physletb.2017.01.011, arXiv:1607.06943.

[61] CMS Collaboration, "Measurements of the pp $\to$ ZZ production cross section and the $Z \to 4\ell$ branching fraction, and constraints on anomalous triple gauge couplings at $\sqrt{s} = 13$ TeV", *Eur. Phys. J. C* **78** (2018) 165, doi:10.1140/epjc/s10052-018-5567-9, arXiv:1709.08601.

[62] T. Sjöstrand, S. Mrenna, and P. Z. Skands, "PYTHIA 6.4 physics and manual", *JHEP* **05** (2006) 026, doi:10.1088/1126-6708/2006/05/026, arXiv:hep-ph/0603175.

[63] M. Bähr et al., "Herwig++ physics and manual", *Eur. Phys. J. C* **58** (2008) 639, doi:10.1140/epjc/s10052-008-0798-9, arXiv:0803.0883.

[64] DELPHI Collaboration, "A study of the b-quark fragmentation function with the DELPHI detector at LEP I and an averaged distribution obtained at the Z pole", *Eur. Phys. J. C* **71** (2011) 1557, doi:10.1140/epjc/s10052-011-1557-x, arXiv:1102.4748.

[65] ALEPH Collaboration, "Study of the fragmentation of b quarks into B mesons at the Z peak", *Phys. Lett. B* **512** (2001) 30, doi:10.1016/S0370-2693(01)00690-6, arXiv:hep-ex/0106051.

[66] S. Dulat et al., "New parton distribution functions from a global analysis of quantum chromodynamics", *Phys. Rev. D* **93** (2016) 033006, doi:10.1103/PhysRevD.93.033006, arXiv:1506.07443.

[67] L. A. Harland-Lang, A. D. Martin, P. Motylinski, and R. S. Thorne, "Parton distributions in the LHC era: MMHT 2014 PDFs", *Eur. Phys. J. C* **75** (2015) 204, doi:10.1140/epjc/s10052-015-3397-6, arXiv:1412.3989.

[68] CMS Collaboration, "Investigations of the impact of the parton shower tuning in PYTHIA8 in the modelling of $\mathrm{t\bar{t}}$ at $\sqrt{s} = 8$ and 13 TeV", CMS Physics Analysis Summary CMS-PAS-TOP-16-021, 2016.

[69] S. Mrenna and P. Skands, "Automated parton-shower variations in PYTHIA8", *Phys. Rev. D* **94** (2016) 074005, doi:10.1103/PhysRevD.94.074005, arXiv:1605.08352.

[70] M. Czakon, D. Heymes, and A. Mitov, "High-precision differential predictions for top-quark pairs at the LHC", *Phys. Rev. Lett.* **116** (2016) 082003, doi:10.1103/PhysRevLett.116.082003, arXiv:1511.00549.

[71] M. Czakon et al., "Top-pair production at the LHC through NNLO QCD and NLO EW", *JHEP* **10** (2017) 186, doi:10.1007/JHEP10(2017)186, arXiv:1705.04105.

[72] S. Catani et al., "Top-quark pair production at the LHC: Fully differential QCD predictions at NNLO", *JHEP* **07** (2019) 100, doi:10.1007/JHEP07(2019)100, arXiv:1906.06535.

[73] CMS Collaboration, "Measurement of differential cross sections for top quark pair production using the lepton+jets final state in proton-proton collisions at 13 TeV", *Phys. Rev. D* **95** (2017) 092001, doi:10.1103/PhysRevD.95.092001, arXiv:1610.04191.

[74] CMS Collaboration, "Measurement of normalized differential $\mathrm{t\bar{t}}$ cross sections in the dilepton channel from pp collisions at $\sqrt{s} = 13$ TeV", *JHEP* **04** (2018) 060, doi:10.1007/JHEP04(2018)060, arXiv:1708.07638.

[75] J. R. Christiansen and P. Z. Skands, "String formation beyond leading colour", *JHEP* **08** (2015) 003, doi:10.1007/JHEP08(2015)003, arXiv:1505.01681.

[76] S. Argyropoulos and T. Sjöstrand, "Effects of color reconnection on $\mathrm{t\bar{t}}$ final states at the LHC", *JHEP* **11** (2014) 043, doi:10.1007/JHEP11(2014)043, arXiv:1407.6653.

[77] CMS Collaboration, "CMS PYTHIA8 colour reconnection tunes based on underlying-event data", 2022. arXiv:2205.02905. Submitted to *Eur. Phys. J. C*.

[78] W. Verkerke and D. P. Kirkby, "The RooFit toolkit for data modeling", in *Proceedings of the 13th International Conference for Computing in High-Energy and Nuclear Physics (CHEP03)*. 2003. arXiv:0306116. [eConf C0303241, MOLT007].

[79] F. James and M. Roos, "Minuit: A system for function minimization and analysis of the parameter errors and correlations", *Comput. Phys. Commun.* **10** (1975) 343, doi:10.1016/0010-4655(75)90039-9.

[80] R. J. Barlow and C. Beeston, "Fitting using finite Monte Carlo samples", *Comput. Phys. Commun.* **77** (1993) 219, doi:10.1016/0010-4655(93)90005-W.

[81] J. S. Conway, "Incorporating nuisance parameters in likelihoods for multisource spectra", in *PHYSTAT 2011*, p. 115. 2011. arXiv:1103.0354. doi:10.5170/CERN-2011-006.115.

[82] ATLAS and CMS Collaborations, "Jet energy scale uncertainty correlations between ATLAS and CMS at 8 TeV", ATL-PHYS-PUB-2015-049, CMS-PAS-JME-15-001, 2015.